Journal of Nuclear Materials 417 (2011) 217–220
DOI: http://dx.doi.org/10.1016/j.jnucmat.2010.12.067

Analytical characterization of secondary phases and void distributions in an ultrafine-grained ODS Fe–14Cr model alloy

V. de Castro [a,*], T. Leguey [a], M.A. Auger [a], S. Lozano-Perez [b], M.L. Jenkins [b]

[a] *Departamento de Física, Universidad Carlos III de Madrid, 28911 Leganés, Spain*
[b] *Department of Materials, University of Oxford, Oxford OX1 3PH, United Kingdom*

Abstract: Two model Fe–14Cr alloys, one containing 0.3 wt.% of Y_2O_3 particles, were fabricated by mechanical alloying of Fe and Cr elemental powders under a He atmosphere. They were subsequently consolidated and thermomechanically treated to produce ultra-fine grained materials. Cr-carbides and oxides were found in both alloys. The oxide dispersion-strengthened (ODS) alloy also contained a fine dispersion of nanoparticles, some of them having a Y–O rich core and a Cr-rich shell. Nanometric sized voids were found in both materials, often attached to secondary phases, dislocations and grain boundaries. Their sizes were significantly smaller in the ODS alloy.

1. Introduction

Low-activation ferritic steels are being considered as candidate materials for use in structural applications in fusion reactors. However, in order to increase the thermal efficiency of the reactor, their operational temperature should be increased. This may be achieved by a uniform dispersion of very fine (1–50 nm) oxide particles, often yttria (Y_2O_3), which are stable at high temperatures. Such oxide dispersions have been shown to increase the high-temperature strength of these materials by two mechanisms; (i) by inhibiting dislocation motion in the metal matrix, and increasing the resistance of the alloy to creep deformation, and (ii) by inhibiting the recovery and recrystallization processes. Another approach to improve the strength, ductility and radiation resistance of steels is to produce nanocrystalline materials with ultra-fine grains. The solution for optimizing the mechanical properties of steels, and moreover to make them more resistant to radiation damage, could be to superimpose the effects of oxide dispersion-strengthening and grain refinement, combined with rigorous control of the microstructure and inclusion cleanliness. The nanoparticles and the large volume fraction of grain boundaries would act as trapping sites for irradiation-induced defects, reducing the radiation induced hardening. The ODS particles could also trap the He and H which result from transmutation reactions in fine bubbles, inhibiting their growth and migration to grain boundaries which can cause the premature failure of the material. The milling atmosphere has proven to play an important role in the final microstructures and mechanical properties of alloys produced by mechanical alloying. For example, Ar–filled cavities and voids have been observed by Transmission Electron Microscopy (TEM) [1,2] and Positron Annihilation Spectroscopy [3] in samples milled under an Ar atmosphere, and the fracture properties of ODS ferritic steels were improved by milling in hydrogen [4]. The effect of the microstructure on the subsequent evolution of the material un-der irradiation has yet to be determined. There have been some previous studies of ODS ferritic and ferritic/martensitic steels mechanically-alloyed in He [5,6], although the void microstructure resulting from the fabrication process and their interaction with particles have not been extensively studied.

This work describes the characterization by analytical TEM of the secondary phases and voids present in an ODS/Fe–14Cr alloy containing 0.3 wt.% Y_2O_3, and a reference Fe–14Cr model alloy produced by milling in He followed by HIP and forging processes.

2. Experimental

The model Fe–14 wt.%Cr ODS and reference alloys were produced by planetary ball milling and consolidated by HIP, forging and subsequent annealing. The alloys were milled in He in order to study the possible formation of He bubbles and their interaction with ODS nanodispersoids. A detailed description of the production process and compositional analyses of the alloys can be found in [7].

TEM samples were prepared by electropolishing 3 mm diameter disks in a TENUPOL 5 twin-jet polisher using 5% $HClO_4$ + 95% CH_3OH as electrolyte. Before each TEM session, the samples were

* Corresponding author. Address: Departmento de Física, Universidad Carlos III de Madrid, Avda. de la Universidad 30, 28911 Leganés, Madrid, Spain. Tel.: +34 916248734.

E-mail addresses: vanessa.decastro@uc3m.es (V. de Castro), leguey@fis.uc3m.es (T. Leguey), mauger@fis.uc3m.es (M.A. Auger), sergio.lozano-perez@materials.ox.ac.uk (S. Lozano-Perez), mike.jenkins@materials.ox.ac.uk (M.L. Jenkins).

additionally cleaned for a few minutes in an ion-beam thinner at 1.5 kV. Bright field (BF) images and microdiffraction patterns were obtained with a Philips CM20 TEM operated at 200 kV and equipped with an X-ray energy-dispersive spectrometer (XEDS). High-angle annular dark-field (HAADF) scanning TEM (STEM) images and XEDS elemental maps were obtained using a JEOL 3000F TEM operated at 300 kV. Energy-filtered TEM (EFTEM) maps were obtained with a JEOL 2200MCO prototype microscope equipped with two spherical aberration (C_s) correctors. The EFTEM series were processed after acquisition using multivariate statistical analysis (MSA) as described in [8].

3. Results and discussion

The general microstructures of the ODS and reference alloys after forging and annealing are described in [7]. The reference alloy had a duplex microstructure consisting of micron and submicron sized grains. This duplex structure was absent in the ODS alloy, in which a totally submicron sized grain structure was achieved. Both alloys contained Cr-rich precipitates as secondary phases (see Section 3.1). In addition, the ODS alloy also contained a nanometric dispersion of Y-rich particles, as described in Section 3.2. Voids were also found in both ODS and reference alloys. They are characterized in Section 3.3.

3.1. Cr-rich precipitates

Precipitates such as those seen in Fig. 1a were found in both alloys. XEDS analyses revealed that they are Cr-rich. They had sizes ranging from 50 to 400 nm and were preferentially observed at grain boundaries, but they were also found within grains. The crystallographic structure of selected precipitates was determined from microdiffraction patterns and high resolution electron microscopy (HREM) images. Most precipitates could be indexed as either Cr_2O_3 oxides or $M_{23}C_6$ (M = Cr, Fe) carbides (see Fig. 1b). These phases are due to the excess of oxygen and the presence of C in the alloys, see [7]. It is very difficult to avoid these impurities, and their presence has been previously reported [1,9].

3.2. ODS nanoparticles

The nanoparticle dispersion was studied by BF-TEM and EFTEM. Particles were mainly distributed in the inner regions of the grains, although they were also observed pinning grain boundaries or dislocations, see Fig. 2. They had sizes ranging between 1 and 30 nm, although most of the particles were below 10 nm. The density of particles was calculated for 4 different regions with average volumes of $200 \times 200 \times 100\ nm^3$. It varies between 0.10 ± 0.02 and 1.5 ± 0.3 ($\times 10^{23}\ m^{-3}$). The foil thicknesses were calculated from EFTEM thickness maps by using the log-ratio method [10]. The inelastic mean free path was estimated from the equation derived by Malis [11].

The particle chemistry was investigated by EFTEM. All the studied nanoparticles were Y-rich and in some of them, a core–shell structure was clearly evident. This consisted of an Y–O rich core and a Cr-rich shell. The shell was visible for particles as small as ~7 nm thick. The presence of nanoparticles with a similar core–shell structure has been recently reported in ODS alloys by EFTEM [8], Atom Probe Tomography [12] and STEM–EDS–EELS [13]. The Y $N_{2,3}$, Cr $M_{2,3}$ and Cr $L_{2,3}$ EFTEM signals were successfully separated and extracted from the background using a multiple-window technique, where an inverse power law was used for background extraction. Both Y $N_{2,3}$ and Cr $M_{2,3}$ signals are clearly observed in Fig. 2b and d. The O K edge is weak and this explains why the O K signal in Fig. 2c was only observed for bigger particles.

3.3. Void distributions and particle-void interaction

Voids probably filled with Helium were found in both the ODS and reference alloys. Helium has a characteristic electron energy loss peak at around 22 eV, which would appear as a small shoulder on the plasmon peak. Although it is a difficult task to separate these two peaks, it is possible to do so, and Izui et al. [14] and more recently Fréchard et al. [15] have used EELS to measure the density of He in individual bubbles. Experimental evidence for the presence of He within bubbles in these alloys is currently under investigation by EELS.

The voids were mainly distributed within the grains and were frequently observed attached to the Y-rich particles in the ODS alloy as well as at dislocations, grain boundaries and Cr-rich precipitates, which were present in both alloys. Examples are shown in Figs. 3 and 4. Fig. 3a is a BF-TEM image showing voids in the matrix and at grain boundaries in the reference alloy. They appear lighter than the background, which is the contrast normally observed for voids larger than ~5 nm in in-focus images. In comparison, Fig. 3b is an HAADF-STEM image of another region in the reference alloy, showing features with a darker contrast than the matrix. The contrast in HAADF images depends on the atomic number Z and in consequence voids (whether filled with He or not) as well as Cr-carbides and oxides embedded in the matrix would all be imaged with a darker contrast than the surrounding matrix. XEDS point analyses were performed in order to distinguish between these

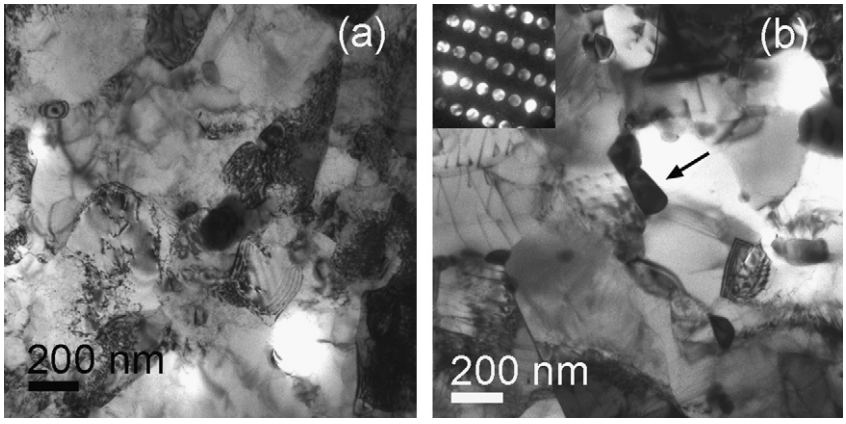

Fig. 1. BF-TEM images showing the distribution of Cr-rich precipitates in (a) the ODS Fe–14Cr alloy and (b) the reference Fe–14Cr alloy. The inset in (b) is a microdiffraction pattern of the precipitate marked with an arrow in the reference alloy, which can be indexed as an $M_{23}C_6$ (M = Cr, Fe) carbide oriented on the ⟨1 1 2⟩ zone axis.

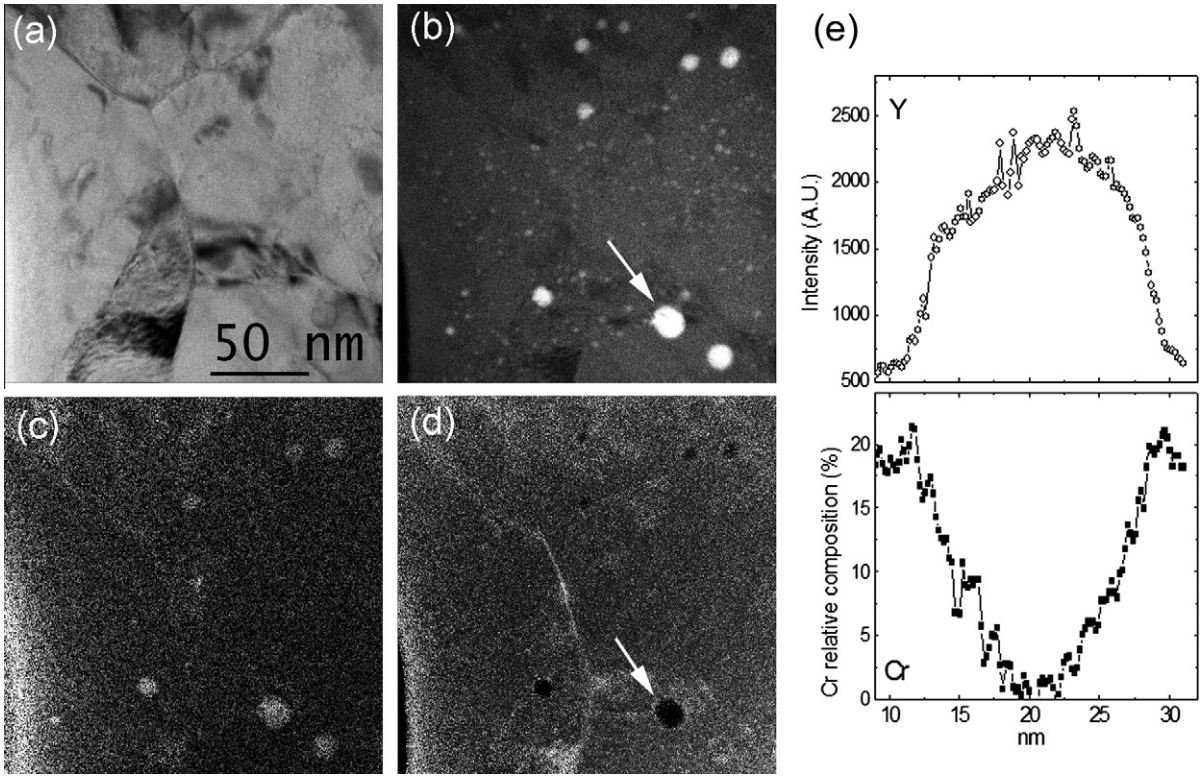

Fig. 2. EFTEM series showing nanoparticles with a core–shell structure in the ODS Fe–14Cr alloy. (a) BF image and (b) Y $N_{2,3}$, (c) O K and (d) Cr $M_{2,3}$ EFTEM elemental maps. (e) Y and Cr intensity profiles across the particle arrowed in (b) and (d) reveal that the Cr signal extends further than the Y signal.

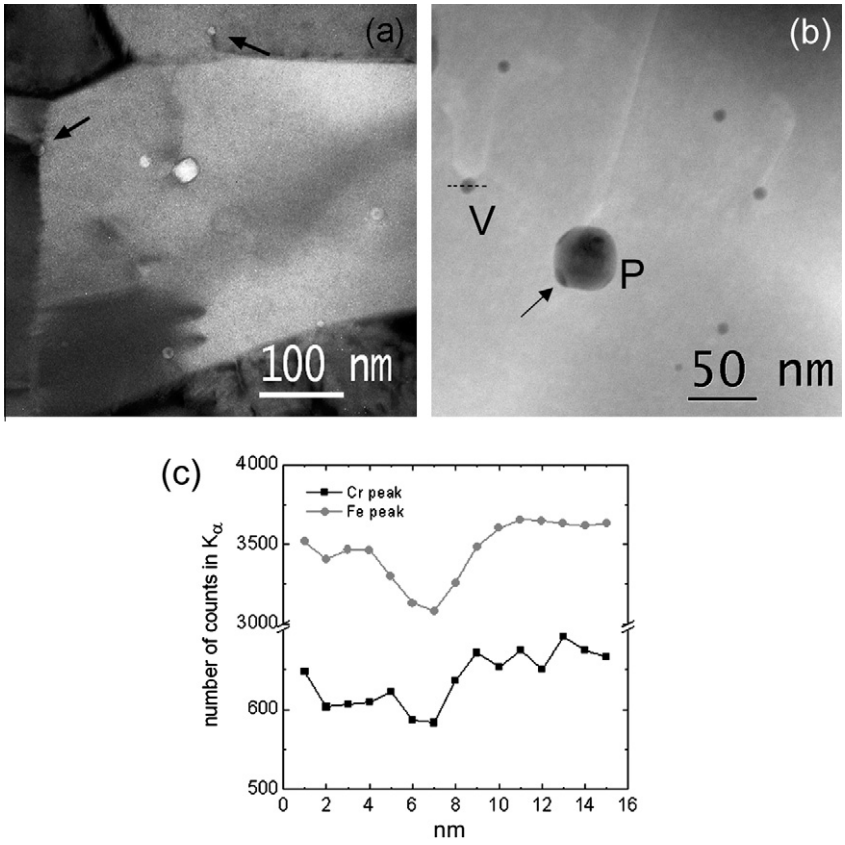

Fig. 3. (a) BF-TEM and (b) HAADF-STEM images showing the distribution of voids and their association with grain boundaries, dislocations and Cr-rich precipitates (marked as "P") in the reference Fe–14Cr alloy (examples arrowed), and (c) intensity profiles of the Fe and Cr K_α XEDS signals along the dashed line through the void marked as "V".

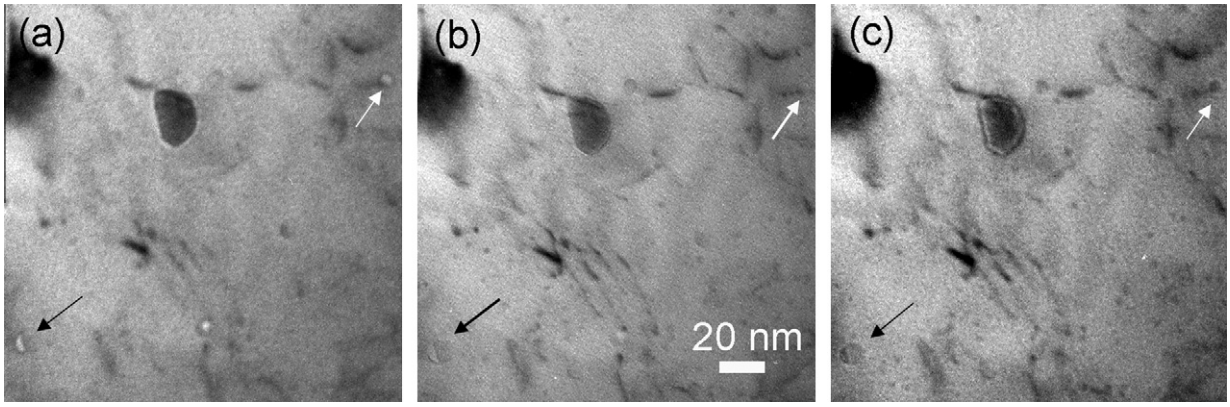

Fig. 4. Through-focal series of small voids attached to particles (white arrow) and dislocations (black arrow) in the ODS Fe–14Cr alloy. (a) Underfocused by 1 m, (b) in-focus, (d) overfocused by 1 m.

possibilities. The results show that only the feature marked as "P" in the figure is a Cr-rich precipitate, while the other dark areas do not present any compositional variations as compared to the matrix. Fig. 3c shows the variation of the intensity of the Fe and Cr K_α signals along a line through the dark area marked as "V". The data represented are the heights of the Gaussian curves adjusted to each peak. The signal intensity is lower when passing through the area, suggesting that it is a void. Similar analyses made for other dark areas in the image yielded similar results. The void den-sity was calculated in this representative region by measuring the thickness from EEL spectra obtained from that area. It was found to be $\sim(5 \pm 1) \times 10^{20}\ m^{-3}$. Further analyses of void densities in both alloys are in progress.

Fig. 4 is a through-focal series showing small voids in the matrix and attached to Y-rich particles in the ODS alloy. These voids were smaller than ~5 nm and in consequence are best imaged out-of-focus [16]. They were observed as bright dots surrounded by dark Fresnel fringes in underfocused images, and as dark dots surrounded by bright Fresnel fringes in overfocused images.

The examples in Figs. 3 and 4 are also representative of the void sizes observed in both samples. The voids were much smaller for the ODS alloy, confirming the importance of nanoparticles as trapping sites for vacancies. Their diameter was estimated from BF-TEM images taken under kinematical conditions by measuring the position of the centre of the principal dark fringe around them in underfocused images, as described in [16]. Most of the voids had sizes ranging between ~5 and 25 nm for the reference alloy, while the observed voids in the ODS alloy were smaller than 5 nm.

4. Conclusions

This paper reports the first analyses of the secondary phases and the void distributions in an ODS Fe–14Cr and a reference Fe14–Cr alloy which were produced by milling in a He atmosphere and consolidated by HIP. Cr-rich carbides and oxides were found in both alloys. The ODS alloy also contained Y-rich nanoparticles, most of them with sizes <10 nm. The chemistry of these particles was studied by EFTEM and the results show that at least some of them consist of an Y–O core surrounded by a Cr-rich shell. Nanometric sized voids were observed in both alloys. They were often found attached to the ODS nanoparticles or the Cr-rich precipitates, as well as at dislocations and grain boundaries. The nanovoids were much smaller in the ODS alloy than in the reference alloy. This is a significant result as it implies that the mechanical performance of ODS alloys may be better than conventional alloys after irradiation in a fusion environment.

Acknowledgements

This research has been supported by the Fusion Energy Materials Science (FEMaS) FP7 coordination action and the IP3 FP6 ESTEEM project under Contract No. 026019. The financial support from European Fusion Development Agreement (Contract No. 09-240), the Ministerio de Innovacion y Ciencia (Project No. ENE 2008-06403-C06-04 and Juan de la Cierva programme) and the Comunidad de Madrid, through the program ESTRUMAT-CM, Grant S-0505/MAT/0077, are also gratefully acknowledged.

References

[1] V. de Castro, T. Leguey, A. Muñoz, M.A. Monge, R. Pareja, E.A. Marquis, S. Lozano-Perez, M.L. Jenkins, J. Nucl. Mater. 386–388 (2009) 449–452.
[2] M. Klimiankou, R. Lindau, A. Möslang, Micron 36 (2005) 1–8.
[3] Y. Ortega, M.A. Monge, V. de Castro, A. Muñoz, T. Leguey, R. Pareja, J. Nucl. Mater. 386–388 (2009) 462–465.
[4] Z. Oksiuta, N. Baluc, J. Nucl. Mater. 386–388 (2009) 426–429.
[5] S. Yamashita, S. Watanabe, S. Ohnuki, H. Takahashi, N. Akasaka, S. Ukai, J. Nucl. Mater. 283–287 (2000) 647–651.
[6] T. Yoshitake, Y. Abe, N. Akasaka, S. Ohtsuka, S. Ukai, A. Kimura, J. Nucl. Mater. 329–333 (2004) 342–346.
[7] M.A. Auger, T. Leguey, A. Muñoz, M.A. Monge, V. de Castro, P. Fernandez, G. Garces, R. Pareja, J. Nucl. Mater. 417 (2011) 213.
[8] S. Lozano-Perez, V. de Castro Bernal, R. Nicholls, Ultramicroscopy 109 (2009) 1217–1228.
[9] Z. Oksiuta, N. Baluc, J. Nucl. Mater. 374 (2008) 178–184.
[10] D.B. Williams, C.B. Carter, Transmission Electron Microscopy, Plenum Press, New York, 1996. p. 678.
[11] T. Malis, S.C. Cheng, R.F. Egerton, J. Electron Micr. Tech 8 (1988) 193–200.
[12] E.A. Marquis, Appl. Phys. Lett. 93 (2008) 181904.
[13] M. Klimenkov, R. Lindau, A. Möslang, J. Nucl. Mater. 386–388 (2009) 553–556.
[14] K. Izui, K. Hojou, S. Furuno, K. Ono, T. Kino, J. Electron Microsc. 33 (1984) 381–383.
[15] S. Fréchard, M. Walls, M. Kociak, J.P. Chevalier, J. Henry, D. Gorse, J. Nucl. Mater. 393 (2009) 102–107.
[16] M.L. Jenkins, M.A. Kirk, Characterization of Radiation damage by Transmission Electron Microscopy, Institute of Physics, 2001.